



Article

<https://doi.org/10.1038/s41567-025-03111-4>

E. coli chemosensing accuracy is not limited by stochastic molecule arrivals

Received: 24 January 2025

Accepted: 23 October 2025

Published online: 08 January 2026

Check for updates

Henry H. Mattingly^{1,8}✉, Keita Kamino^{2,3,4,8}, Jude Ong⁵, Rafaela Kottou⁵, Thierry Emonet^{1,5,6,7}✉ & Benjamin B. Machta^{1,6,7}✉

Organisms use specialized sensors to measure their environments, but the principles governing their accuracy are unknown. The bacterium *Escherichia coli* climbs chemical gradients at speeds bounded by the amount of information it receives from its environment. However, it remains unclear what prevents *E. coli* cells from acquiring more information. Past work argued that chemosensing by *E. coli* is limited by the stochastic arrival of molecules at their receptors by diffusion, without providing direct evidence. Here we show instead that *E. coli* encode two orders of magnitude less information than this physical limit. We develop an information-theoretic approach to quantify how accurately chemical signals can be estimated from observations of molecule arrivals as the physical limit and of chemotaxis signalling activity for *E. coli* cells, and then we measure the associated information rates in single-cell experiments. Our findings demonstrate that *E. coli* chemosensing is limited by internal noise in signal processing rather than molecule arrival noise, motivating investigations of the physical and biological constraints that shaped the evolution of this prototypical sensory system.

Evolution selects function, and therefore, living systems are shaped by complex fitness objectives and constraints. This has motivated the use of normative theories, subject only to the constraints of physics, to derive fundamental limits on function and to rationalize the design of biological systems^{1–8}. This approach has been especially successful in the context of information processing, a hallmark of living systems, where theories of optimal estimation can be brought to bear^{6,9,10}. However, biology implements information processing using non-ideal components, in the confines of a body and with limited resources, which introduce system-specific constraints^{10–14}. Determining what bounds or constraints meaningfully limit information processing in a particular system would shed light on the forces that have shaped its evolution and inform our understanding of biological information processing more broadly.

Escherichia coli chemotaxis is an ideal system for studying the limits of biological information processing^{15,16}. *E. coli* climb chemical

gradients by alternating between straight-swimming runs and randomly reorienting tumbles¹⁷. As they swim, they measure the time-dependent concentration of attractant along their trajectory, $c(t)$, using transmembrane receptors, encode these measurements into the activity of intracellular, receptor-associated CheA kinase activity $a(t)$ and act on these measurements to decide when to tumble (Fig. 1). Importantly, chemotaxis provides a fitness advantage in structured chemical environments¹⁸.

Recently, we asked how fast an ideal bacterium could climb a gradient with the information it gets about its chemical environment, and how *E. coli* compare with this theoretical performance bound⁸. We found that although typical *E. coli* cells get very little information about chemical signals—about 0.01 bits per second in a centimetre-long gradient—they climb gradients at speeds near the theoretical maximum with the information they get. Thus, *E. coli* chemotaxis is information-limited.

¹Center for Computational Biology, Flatiron Institute, New York City, NY, USA. ²Institute of Molecular Biology, Academia Sinica, Taipei, Taiwan. ³Institute of Physics, Academia Sinica, Taipei, Taiwan. ⁴Institute of Physics, National Yang Ming Chiao Tung University, Taipei, Taiwan. ⁵Molecular, Cellular, and Developmental Biology, Yale University, New Haven, CT, USA. ⁶Department of Physics, Yale University, New Haven, CT, USA. ⁷QBio Institute, Yale University, New Haven, CT, USA. ⁸These authors contributed equally: Henry H. Mattingly, Keita Kamino. ✉e-mail: Hmattingly@flatironinstitute.org; Thierry.emonet@yale.edu; Benjamin.machta@yale.edu

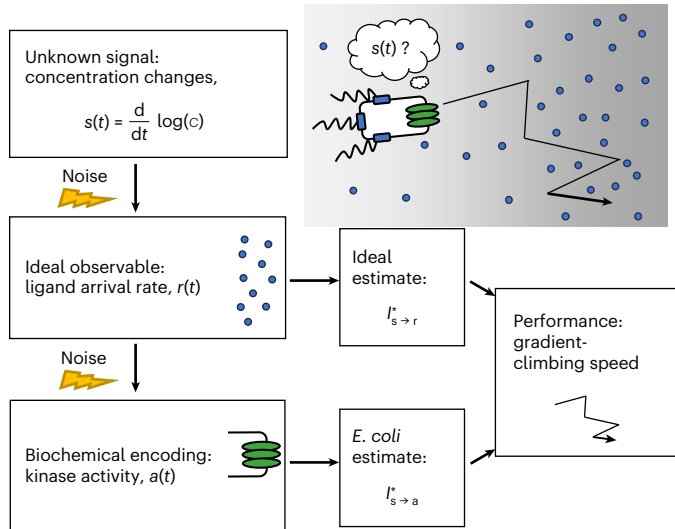


Fig. 1 | Is the sensing accuracy of *E. coli* set by physical limits or internal constraints? To climb chemical gradients, *E. coli* need to accurately estimate an unknown signal: the rate of change of attractant ligand concentration, $s(t) = \frac{d}{dt} \log(c(t))$ (ref. 8). Top right: grey shading is concentration. The first physically observable quantity is the stochastic rate at which ligand molecules (blue dots) arrive at the cell receptors, $r(t)$. Thus, the physical limit on chemosensing, and in turn gradient-climbing speed, is set by how accurately $s(t)$ can be estimated from the time series of past $r(t)$, quantified by an information rate, $I_{s \rightarrow r}^*$. *E. coli* sense ligand arrivals with transmembrane receptors and respond with changes in the activity of intracellular CheA kinases, $a(t)$ (green). The accuracy with which the signal can be estimated from kinase activity is quantified by another information rate, $I_{s \rightarrow a}^*$. As kinase activity is stochastic, the sensing accuracy and gradient-climbing speed of *E. coli* must be below the physical limit, but how much less?

This raises the question: why do *E. coli* not get more information and, thus, climb gradients faster? One possibility is that they are limited by physics. The first physically measurable quantity is the rate of ligand molecule arrivals at the cell receptors by diffusion, $r(t)$ (Fig. 1). Berg and Purcell² demonstrated that the stochasticity of this arrival rate limits the accuracy of any estimate of chemical concentration $c(t)$, thus inspiring an entire field of biophysics^{6,10,11,19–26}. They and others further argued that bacteria approach this physical limit, a widely held understanding in the field. However, no direct comparison between bacterial chemosensing and physical limits has been made because it is unclear how to quantify the uncertainty of a cell regarding external signals.

Directly answering whether physical limits or internal constraints prevent chemotaxing *E. coli* from acquiring more information faces several general challenges. First, not all environmental signals are useful for function. For chemotaxis in shallow gradients, we recently showed that the time derivative of (log) concentration, $s(t) = \frac{d}{dt} \log(c)$ – rather than concentration $c(t)$ itself – is the ‘behaviourally relevant’ signal⁸. Second, cells do not need to represent their estimates of relevant signals in a straightforward way. In *E. coli*, CheA kinase activity depends on external signals, but $a(t)$ is not necessarily the estimate made by the cell of $s(t)$, and variation in $a(t)$ is not the uncertainty of the cell regarding $s(t)$. Signals are, instead, encoded in the dynamics of the intermediate variables in the cell and decoded by downstream processing. Third, probing a cell’s encoding of time-varying signals requires dynamic measurements of both the environment and responses in single cells, which was recently made possible by single-cell Förster resonance energy transfer (FRET)^{8,27–31}.

Here we address these challenges and determine whether *E. coli* chemosensing approaches the physical limits. To make this question experimentally testable, we asked how accurately the signal $s(t)$ can

be inferred from molecule arrivals, which sets the physical limit, versus from kinase activity, the quantity accessible to the cell. Inference accuracy in each case takes the form of an information rate (Fig. 1). Then, we quantified these information rates using single-cell FRET measurements in several background concentrations. We found, surprisingly, that a typical *E. coli* cell gets orders of magnitude less information than the physical limit. This is because the signal transduction noise in *E. coli* far exceeds molecule arrival noise, and we conclude that their information processing during chemotaxis is internally limited. As a consequence, we predict that *E. coli* climb gradients much more slowly than the physical limits on chemosensing allow, and support this with simulations. These results raise questions about what specific constraints limit chemosensing by *E. coli*, and more broadly, they motivate consideration of the physical and biological constraints on information processing.

Physical limit on behaviourally relevant information due to the stochastic arrival of molecules

To climb chemical gradients, *E. coli* must encode information about $s(t)$ so that it can be read out by the motors⁸ (Supplementary Sections 1 and 2). An ideal agent would estimate $s(t)$ and make navigation decisions based on perfect observations of past particle arrivals $\{r\}$ (Fig. 1). The behaviourally relevant information about the signal $s(t)$ thus acquired from past particle arrivals $\{r\}$ is quantified by the following transfer entropy rate³²:

$$I_{s \rightarrow r}^* \equiv \lim_{dt \rightarrow 0} \frac{1}{dt} I(r(t+dt); s(t)|\{r\}), \quad (1)$$

where $I(X; Y|Z)$ is the mutual information between X and Y conditioned on Z (ref. 33). This quantity obeys a data-processing inequality³³ in the context of bacterial chemotaxis in shallow gradients, where feedback from behaviour onto signals is negligible^{34,35} (Supplementary Section 3). Therefore this quantity sets the physical limit on information available in any downstream encoding of the signal.

The form of the physical limit in equation (1) is unknown. To derive it, we first need a dynamical model for the signal and the particle arrival rate (Supplementary Section 4). In static gradients, the signals a cell experiences are determined by its own run-and-tumble motion in the gradient. Accordingly, in a gradient of steepness $g = d \log(c)/dx$, the signal is $s(t) = gv_x(t)$, where v_x is the up-gradient velocity of the cell. In shallow gradients, where weak signals have small effects on run-and-tumble statistics, we can approximate $s(t)$ as Gaussian with correlation function $\langle s(t)s(t') \rangle = g^2 V(t-t') \approx g^2 \sigma_v^2 \exp(-\frac{|t-t'|}{\tau_v})$, to leading order in g (refs. 8,12). Here $V(t)$ is the correlation function of v_x in the absence of a gradient; σ_v^2 is the variance of v_x , which depends on the swimming speed of the cell, and τ_v is the signal correlation time, which depends on the mean run duration of the cell, the persistence of tumbles and rotational diffusion⁸.

Molecule arrival events follow a Poisson process with time-varying rate $\langle r(t) \rangle = k_D c(t) = 4Dl c(t)$, where $D \approx 800 \mu\text{m}^2 \text{s}^{-1}$ (ref. 36) is the diffusivity of the ligand and l is the radius of a circular sensor on the surface of the cell^{2,24}. We choose $l \approx 60 \text{ nm}$ (ref. 37) to match the size of the receptor array in the cell membrane of *E. coli*. These give $k_D \approx 1.2 \times 10^5 \text{ s}^{-1} \mu\text{M}^{-1}$, comparable to previous estimates^{2,38}. If many molecules arrive per run, $r_0 \tau_v \gg 1$, we can approximate the Poisson process with a Gaussian process for the number of molecule arrivals per unit time, $r(t) = k_D c(t) + \sqrt{r_0} \xi(t)$. Here $r_0 = k_D c_0$ is the background molecule arrival rate, c_0 is the background concentration and the noise is $\langle \xi(t) \xi(t') \rangle = \delta(t-t')$, where $\delta(t-t')$ is the Dirac delta function. We assume the sensor absorbs every molecule it senses², but allowing rebinding events lowers the limit by only an $O(1)$ prefactor^{24,25}.

As $s(t)$ and $\{r\}$ are approximately Gaussian, the physical limit in equation (1) depends only on the posterior variance $\sigma_{s|r}^2$ of $s(t)$ given past particle arrivals $\{r\}$ (Supplementary equation (23)), which can be

derived using causal Wiener filtering^{12,39–42} (Supplementary Sections 5 and 6). We find that the physical limit on behaviourally relevant information for chemotaxis in shallow gradients is

$$\hat{I}_{s \rightarrow r}^* \approx \frac{1}{\tau_v} \rho_{rs}^2 \approx \frac{1}{\tau_v} \frac{1}{4} \gamma_r, \quad (2)$$

where ρ_{rs} is the Pearson correlation coefficient between the true signal $s(t)$ and the optimal estimator of $s(t)$ constructed from past molecule arrivals, $\hat{s}_r(t)$ (Supplementary Section 7). Here we defined the dimensionless signal-to-noise ratio of molecule arrivals, $\gamma_r = 2r_0 g^2 \sigma_v^2 \tau_v^3$. Equation (2) is valid when $\gamma_r \ll 1$, which sets the small-signal regime for $\hat{I}_{s \rightarrow r}^*$. See Supplementary equation (46) for the general expression and Supplementary Fig. 5 for validation. Increasing the background r_0 , the gradient steepness g or the swimming speed σ_v increases the signal-to-noise ratio of molecule arrivals. Longer runs, τ_v , also increase $\hat{I}_{s \rightarrow r}^*$ by allowing more time to average out noise. In Supplementary Section 8, we also derive and discuss the optimal kernel for constructing $\hat{s}_r(t)$. We expect spatial sensing across the cell body to be negligible compared with temporal sensing, as argued by Berg and Purcell (Supplementary Section 9).

Relevant information encoded in kinase activity

We next derive $\hat{I}_{s \rightarrow a}^*$, which quantifies how well $s(t)$ can be estimated from the dynamics of kinase activity. For this, we need models of kinase responses to ligand arrivals and noise in kinase activity (Supplementary Section 10). In shallow gradients, we use linear^{8,43}, Gaussian theory, which has been validated experimentally^{8,27,28} and computationally⁴⁴. For a cell with steady-state kinase activity a_0 in background r_0 , kinase responses follow:

$$a(t) = a_0 - \int_{-\infty}^t K_r(t-t') (r(t') - r_0) dt' + \eta_n(t). \quad (3)$$

E. coli respond to a step increase in attractant concentration with a fast drop in kinase activity, followed by slow adaptation back to the pre-stimulus level¹⁵. We model this phenomenologically with response function $K_r(t) = G_r \left(\frac{1}{\tau_1} \exp(-\frac{t}{\tau_1}) - \frac{1}{\tau_2} \exp(-\frac{t}{\tau_2}) \right) \Theta(t)$, where G_r is the gain of the response to molecule arrival rate r , τ_1 is the fast response time, τ_2 is the slow adaptation time and $\Theta(t)$ is the Heaviside step function. Kinase responses can equivalently be expressed in terms of past signals s , with a related kernel $K(t)$ that we used previously⁸ ($K_r(t) = \frac{1}{r_0} \frac{d}{dt} K(t)$; Supplementary equation (68)).

Noise in kinase activity is driven by a combination of stochastic molecule arrivals and internally driven fluctuations. Previous single-cell FRET experiments have observed large, slow fluctuations in kinase activity $\eta_n(t)$ on a timescale of 10 s (refs. 8,27,28,45). These are described well as Gaussian, with correlation function $\langle \eta_n(t) \eta_n(t') \rangle = D_n \tau_n \exp(-\frac{|t-t'|}{\tau_n})$. Here D_n is the diffusivity of internal noise in kinase activity, and τ_n is its correlation time. In addition, equation (3) has additive noise arising from responses to molecule arrival noise. To date, it has not been possible to measure kinase fluctuations on timescales shorter than the CheY-CheZ relaxation time τ_1 , but it cannot go below the level set by responses to molecule arrival noise. Thus, the phenomenological model above agrees with experiments at low frequencies while obeying known physics at high frequencies.

As above, evaluating $\hat{I}_{s \rightarrow a}^*$ again reduces to deriving the posterior variance $\sigma_{s|a}^2$ of the signal $s(t)$ given past kinase activity $\{a\}$ (Supplementary Section 11). Furthermore, previous measurements (and measurements below) show that $\tau_1 \ll \tau_v$ ^{8,46,47} and that $\tau_2 \approx \tau_n \gg \tau_1$ (ref. 8). Thus, in shallow gradients, the information encoded in kinase activity is

$$\hat{I}_{s \rightarrow a}^* \approx \frac{1}{\tau_v} \rho_{sa}^2 \approx \frac{1}{\tau_v} \frac{1}{4} \gamma_a \frac{\gamma_r / \gamma_a}{(1 + \sqrt{\gamma_r / \gamma_a})^2}, \quad (4)$$

where ρ_{sa} is the Pearson correlation coefficient between the true signal $s(t)$ and the optimal estimator of $s(t)$ constructed from past kinase activity, $\hat{s}_a(t)$. We define the dimensionless kinase activity signal-to-noise ratio $\gamma_a = \frac{G_r}{D_n} r_0^2 g^2 \sigma_v^2 \tau_v$. Equation (4) is valid when $\gamma_a \ll 1$, which sets the small-signal regime for $\hat{I}_{s \rightarrow a}^*$. See Supplementary equation (98) for the general expression and Supplementary Fig. 5 for validation. An ideal sensor with no internal noise corresponds to $\gamma_a \rightarrow \infty$, giving $\hat{I}_{s \rightarrow a}^* = \hat{I}_{s \rightarrow r}^*$. Conversely, internal noise degrades information about the signal, and the information rate becomes $\hat{I}_{s \rightarrow a}^* \approx \frac{1}{\tau_v} \frac{1}{4} \gamma_a$ as $\gamma_a / \gamma_r \rightarrow 0$. In Supplementary Section 12, we derive and discuss the optimal kernel for constructing $\hat{s}_a(t)$.

Single-cell measurements constrain signal and kinase properties

To quantify the information rates above, we then performed single-cell experiments to measure the parameters characterizing the signal statistics, kinase response function and kinase noise statistics. As the attractant, we used aspartate (Asp), to which *E. coli* respond with the highest sensitivity among known attractants⁴⁸.

To quantify the signal statistics, we recorded trajectories of cells swimming in several background concentrations of Asp: $c_0 = 0.1 \mu\text{M}$, $1 \mu\text{M}$ and $10 \mu\text{M}$ (Fig. 2a). Single cells in the clonal population exhibited a range of phenotypes^{45,49–56}. Therefore, as before⁸, we focused on a typical cell by estimating the median single-cell parameter values in the population. In particular, we binned cells by the fraction of time spent running P_{run} and computed $V(t)$ among cells with the median P_{run} . The parameters σ_v^2 and τ_v in each background c_0 were then estimated by fitting $V(t)$ with a decaying exponential. These parameters depended weakly on c_0 , and their values in $c_0 = 1 \mu\text{M}$ were $\sigma_v^2 = 146 \pm 5 (\mu\text{m s}^{-1})^2$ and $\tau_v = 1.19 \pm 0.01 \text{ s}$ (see Supplementary Fig. 1a,b for all values).

We measured kinase response functions as before⁸, using a microfluidic device in which we could deliver controlled chemical stimuli²⁹. Cells immobilized in the device were delivered ten small positive and negative step changes of Asp concentration around several backgrounds, c_0 (Fig. 2b). Kinase responses were measured in single cells with FRET^{27–31,57} between CheZ-mYFP and CheY-mRFP1. Then we fitted the average response of each cell to $K_r(t)$ above and computed the population-median parameter values. As τ_1 estimated this way includes the relatively slow dynamics of CheY-CheZ interactions, we used $\tau_1 = 0$ in the calculations below, which only slightly overestimates $\hat{I}_{s \rightarrow a}^*$. The adaptation time τ_2 depended weakly on c_0 (in $c_0 = 1 \mu\text{M}$ $\tau_2 = 7.4 \pm 0.3 \text{ s}$) (Supplementary Fig. 1d), but G_r varied considerably: for $c_0 = \{0.1, 1, 10\} \mu\text{M}$, we measured $G_r = \frac{1}{k_D} \{3.2 \pm 0.1, 2.28 \pm 0.05, 0.251 \pm 0.009\}$ (Supplementary Fig. 1e,f).

The dependence of G_r on c_0 was consistent with the Monod-Wyman-Changeux (MWC) model for kinase activity^{15,58–60}, which captures numerous experimental measurements^{29,31,57,61,62}. In particular, $G_r = \frac{1}{r_0} G(c_0)$, where $G(c_0) \approx G_\infty \frac{c_0}{c_0 + K_i}$ is the MWC gain, K_i is the dissociation constant of two-state receptors for Asp when in their inactive state and G_∞ is a constant (Supplementary Section 10). Thus, in the ‘linear-sensing’ regime ($c_0 \ll K_i$), the gain is constant, $G_r = G_\infty \frac{1}{k_D K_i}$, and in the ‘log-sensing’ regime ($c_0 \gg K_i$)^{63,64}, the gain decreases with the background, $G_r \approx G_\infty / r_0$. Fitting the measured G_r to the MWC model gave $G_\infty = 3.5 \pm 0.1$ and $K_i = 0.81 \pm 0.04 \mu\text{M}$.

Finally, we estimated the parameters of slow kinase fluctuations by measuring kinase activity in single cells experiencing constant Asp concentrations c_0 (Fig. 2c). The diffusivity D_n and timescale τ_n of these fluctuations were extracted from each time series using Bayesian filtering^{8,65}. We then computed the population-median parameter values. Both of these parameters depended weakly on c_0 , and their

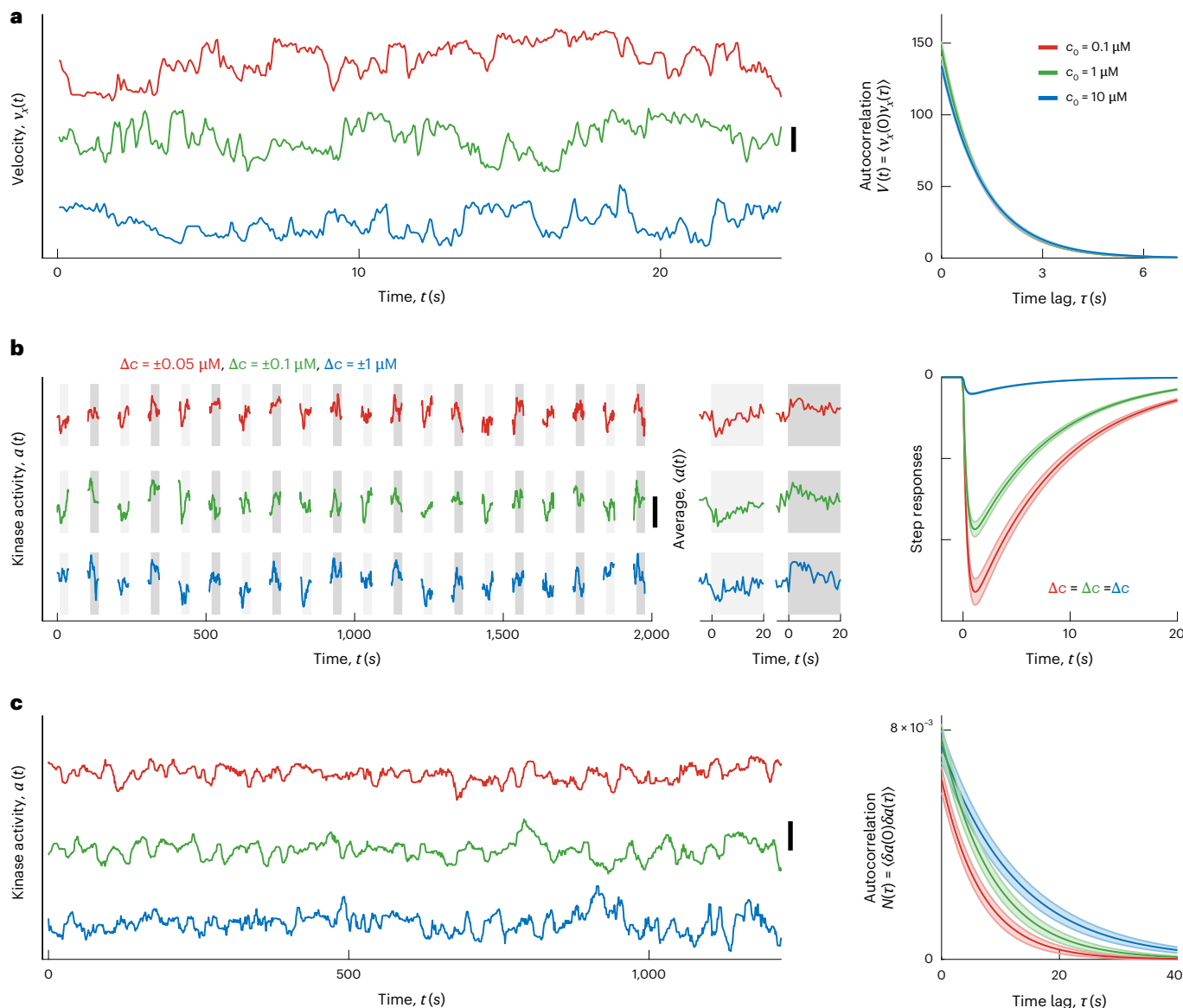


Fig. 2 | Signal statistics, kinase responses and kinase fluctuations in different ligand concentrations. **a**, Signal statistics. Left: representative time series of up-gradient velocity v_x from three individual cells, one in each Asp concentration c_0 . Cells were binned by the fraction of time spent running P_{run} . The velocity autocorrelation function $V(t)$ was computed by averaging over cells with the median P_{run} . The parameters of $V(t)$ were extracted by fitting a decaying exponential to the data. Right: $V(t)$ model fits for each c_0 . The curves are on top of each other. Vertical axis units are $(\mu\text{m s}^{-1})^2$. Throughout, shading indicates the predictions of the fitted model with population-median parameter values \pm s.e.m., and line colours indicate c_0 : 0.1 μM (red), 1 μM (green) and 10 μM (blue). Throughout, at least 3 biological replicates, with at least 80 individual cells each, were performed per background concentration. **b**, Linear responses. Left: kinase activity was measured by FRET in blocks of 25 s, separated by 65 s without illumination. In each block, after 5 s, the concentration was stepped up

(light grey shading) or down (dark grey shading) around c_0 , then maintained for 20 s, then returned to c_0 . Concentration step sizes Δc were different for each c_0 (shown above the panel). Shown are three representative cells, one for each c_0 . Middle: average responses of the cells in the left panel to steps up (light grey) and steps down (dark grey). Single-cell responses were fitted to extract parameters of the response function $K_r(t)$. Right: model fits for kinase responses to a fixed step size Δc , using population-median parameters. The gain G_r decreases with c_0 . **c**, Noise statistics. Left: fluctuations in kinase activity were measured in constant background concentrations. Representative time series from three cells are shown, one for each c_0 . Parameters of the slow noise autocorrelation function were fitted to single-cell traces using Bayesian filtering^{8,65}. Right: estimated noise autocorrelation functions with population-median parameters. Vertical axis units are kinase activity squared. Scale bars, 20 $\mu\text{m s}^{-1}$ (**a**, right axis), 0.3 (**b,c**, right axis).

values in $c_0 = 1 \mu\text{M}$ were $D_n = 8.1 \pm 0.9 \times 10^{-4} \text{ s}^{-1}$ and $\tau_n = 8.7 \pm 0.9 \text{ s}$ (see Supplementary Fig. 1c,d for all values).

Comparing *E. coli* with the physical limit

Both the information rate for *E. coli*, $I_{s \rightarrow a}^*$, and the physical limit, $I_{s \rightarrow r}^*$, are proportional to g^2 in shallow gradients. Therefore, using the measured parameters, we plotted the information rates per g^2 as functions of c_0 (Fig. 3a), for values of g in which we previously measured the

gradient-climbing speeds of *E. coli*⁸. Doing so reveals that *E. coli* are surprisingly far from the physical limit: in shallow gradients, $I_{s \rightarrow a}^*$ is at least two orders of magnitude below $I_{s \rightarrow r}^*$ across all background concentrations.

To quantify this comparison, we computed the ratio of the information rate for *E. coli* and the physical limit, $\eta \equiv I_{s \rightarrow a}^*/I_{s \rightarrow r}^*$ (Fig. 3b, small error bars). In vanishingly small gradients (black curve), η is independent of g . In this regime, $I_{s \rightarrow r}^* \propto c_0$ in all background concentrations, and

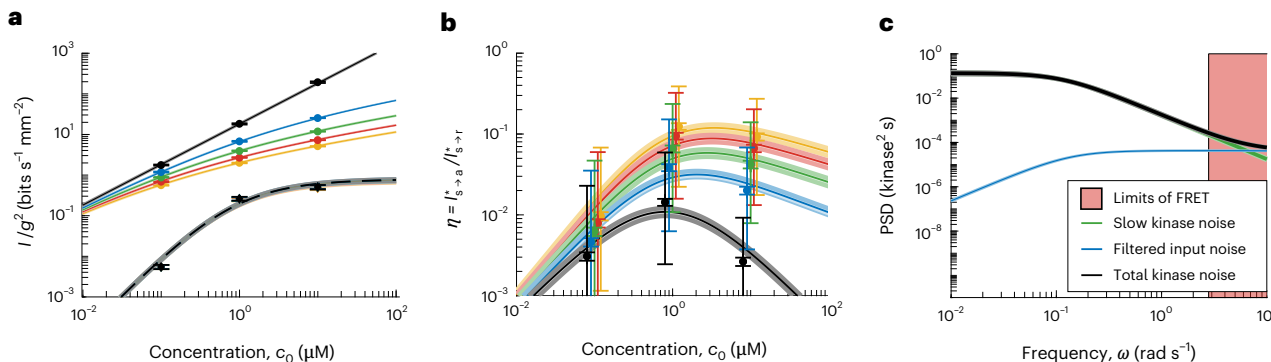


Fig. 3 | Comparing the sensing accuracy of *E. coli* with the physical limit.

a. Information rates per gradient steepness squared g^2 , namely from molecule arrival rate, $I_{s \rightarrow r}^*$ (Supplementary equation (46); solid lines) and kinase activity, $I_{s \rightarrow a}^*$ (Supplementary equation (98); dashed lines) use the MWC model gain G_r (Supplementary equation (99)) and remaining parameters measured in $c_0 = 1 \mu M$) for gradients of various steepnesses, $g \in \{0^+, 0.1, 0.2, 0.3, 0.4\} mm^{-1}$, in black, blue, green, red and yellow, respectively, where 0^+ is the limit of an infinitely shallow gradient. Dots are experimental measurements. Error bars and shading are the s.e.m. around the population-median values. *E. coli* are far from the physical limit when signals are weak and sensor quality matters. **b.** $\eta = I_{s \rightarrow a}^*/I_{s \rightarrow r}^*$ versus c_0 . Colours and

markers are the same as in **a**. Shading and small error bars on the dots are the s.e.m. Large error bars on the dots are estimates of 95% confidence intervals of population variation in η , assuming that swimming, kinase response and kinase noise parameters are uncorrelated. Dots are shifted slightly for visual clarity. **c.** Fitted models for the PSDs of noise sources in $c_0 = 1 \mu M$. Green: slow noise in kinase activity. Blue: molecule arrival noise filtered through the kinase response function. Black: sum of green and blue. Red shading: experimentally inaccessible timescales using CheY–CheZ FRET. See also Supplementary Fig. 3 and Supplementary Section 10.

the shape of η is determined by the gain of the kinase response, G_r . When $c_0 \ll K_i$, the gain is constant and η increases with background, $\eta \propto c_0$. When $c_0 \gg K_i$, G_r decreases and outweighs the increasing c_0 , so $\eta \propto 1/c_0$. These two regimes are separated by a peak at $c_0 = K_i$, where $\eta \approx 0.014 \pm 0.002$ at our closest measurement. As the gradient gets steeper, η increases, up to $\eta \approx 0.1$ when $g = 0.4 mm^{-1}$. This larger value of η does not mean that *E. coli* counts nearly every molecule in steeper gradients. Instead, the physical limit saturates (solid lines decreasing with g in Fig. 3a). Thus, in a steep gradient, even a poor sensor can infer the signal with decent accuracy.

Although typical cells are far from the sensing limit, non-genetic diversity in sensing and swimming phenotypes^{49,55,62} could cause a significant fraction of cells in a population to approach the limit. Our experimental set-up did not allow us to measure all parameters in the same single cells, but we did measure single-cell parameters from different cells. Assuming that the swimming, kinase responses and kinase noise parameters are uncorrelated across cells, we use a maximum-likelihood approach to estimate the variability of η in the population (Supplementary Section 13). This analysis indicates that although the 95th percentile of the population can be ~5 times closer to the physical limit than the median cell, they are still far from it (Fig. 3b, large error bars).

Figure 3c shows the power spectral density (PSD) of slow noise in kinase activity (green line) compared with the PSD of filtered molecule arrival noise (blue line) in $c_0 = 1 \mu M$. If *E. coli* were close to the physical limit, nearly all noise in kinase activity would come from filtered molecule arrivals. Instead, slow kinase fluctuations are much larger over the range of frequencies observable in the experiment. Thus, chemosensing by *E. coli* is limited by constraints on its internal signal processing rather than the external physics of ligand diffusion.

Consistent with this, the optimal signal estimate constructed from simulations of kinase activity $\hat{s}_a(t)$ is visibly lower quality than that from particle arrivals $\hat{s}_r(t)$ (Fig. 4a). The implication for chemotaxis is that an ideal cell would climb gradients much faster than *E. coli*. We tested this prediction in simulations where the tumble rates of ideal and *E. coli* cells depended on their current estimates of the signal, $\hat{s}_r(t)$ and $\hat{s}_a(t)$, respectively. For fair comparison, the estimates were scaled to have the same variance, so that the only difference in the chemotaxis behaviour of the two populations was the accuracy of their estimates (Supplementary Section 14). Figure 4b shows that ideal cells (blue) climb gradients much faster than *E. coli* cells (green). In Fig. 4c, we trace

this back to the loss of behaviourally relevant information by *E. coli*. Our previous theory⁸ predicts that the ratio of the drift speed of *E. coli*, v_a , to the drift speed of an ideal cell v_i is $v_a/v_i = \sqrt{I_{s \rightarrow a}^*/I_{s \rightarrow r}^*}$, and plotting these ratios against each other in Fig. 4c shows good agreement. Thus, *E. coli* probably climbs gradients much slower than the physical limit on chemosensing allows, and it may be possible to evolve or engineer a microswimmer that, with the same signal-to-noise ratio γ_r , climbs gradients much faster than *E. coli*.

Discussion

Our findings are contrary to the long-standing belief that chemosensing by *E. coli* approaches the physical limit. Berg and Purcell's argument for optimality by *E. coli* assumed that cells must estimate the change in concentration over a single run Δc with uncertainty less than Δc (equation (57) in ref. 2). Using their physical limit, they computed the minimum required averaging time T for this condition to be met and found that measured bacterial run durations were slightly longer than the minimum T . Thus, they argued that chemotaxis would be impossible with shorter runs and that the bacterial chemotaxis machinery is nearly optimal. However, *E. coli* do not necessarily need to exceed a stringent signal-to-noise threshold in each run. Instead, as the displacements of cells accumulate over many runs, they climb gradients on average even when individual tumble decisions are inaccurate, with no hard threshold on accuracy. Berg and Purcell's threshold condition can be written as $\gamma_r > 16/3$ (Supplementary Section 15), but both the ideal cells and the *E. coli* simulated in Fig. 4b climb the gradient when $g = 0.05 mm^{-1}$, $c_0 = 1 \mu M$ and $\gamma_r = 0.15 \ll 16/3$.

Ref. 38 found that the marine bacterium *Vibrio ordalii* senses chemical signals with accuracy within a factor of ~6 of the physical limit. The model in that study assumed cells infer $s(t)$ in independent time windows of duration $T = 0.1 s$. However, the signal is correlated over a time $\tau_v > T$, so an ideal agent can average out molecule arrival noise for times up to τ_v . This increases the theoretical limit and, thus, the distance of *V. ordalii* from it by a factor $(\tau_v/T)^3 = (0.45 s/0.1 s)^3 \approx 90$, due to the τ_v^3 in γ_r (equation (2); related to T^3 in ref. 21). This suggests that chemosensing in other bacterial species may also be internally limited.

Why are *E. coli* so far from the physical limit? One possibility is the physical implementation of their sensory system may impose trade-offs. For example, the need to operate over a wide range of

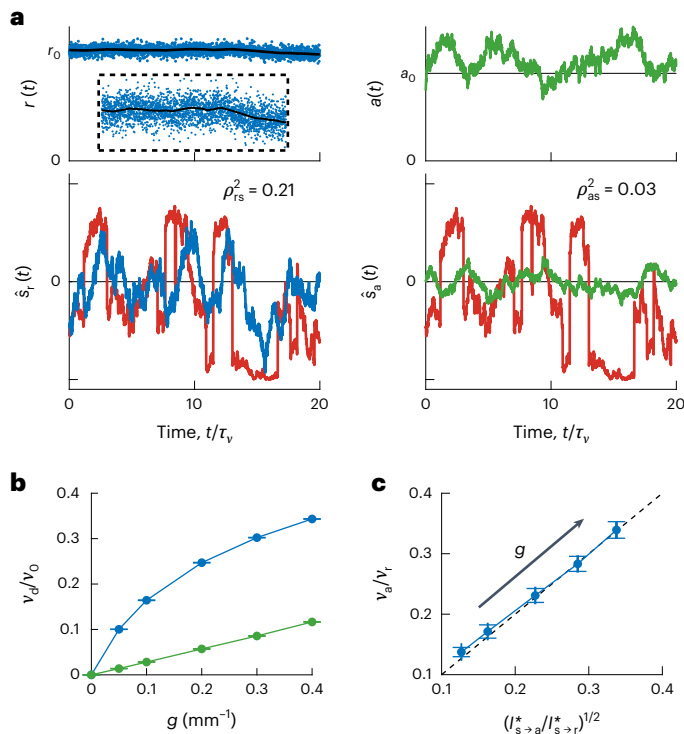


Fig. 4 | Consequences of *E. coli* being far from the physical limit on sensing.

a, Simulation of run-and-tumble motion in a concentration gradient and optimal signal estimates using measured parameters (Supplementary Fig. 1; background $c_0 = 1 \mu\text{M}$, gradient $g = 0.4 \text{ mm}^{-1}$). Top left: an ideal cell directly observes the molecule arrival rate $r(t)$ (blue dots). The black line is the mean, $\langle r(t) \rangle = k_D c(t)$, where k_D is the mean particle arrival rate per unit concentration, and $r_0 = k_D c_0$. Time is scaled by the signal correlation time τ_v . Inset: the entire trajectory zoomed in to show the subtle changes in $c(t)$. Bottom left: optimal signal estimate from molecule arrivals $\hat{s}_r(t)$ (blue) overlaid on the true signal $s(t)$ (red). Top right: simulated *E. coli* respond to molecule arrivals with changes in kinase activity (green). Bottom right: optimal signal estimate from kinase activity $\hat{s}_a(t)$ (green) overlaid on the true signal $s(t)$ (red). $\hat{s}_a(t)$ is visibly of lower quality than $\hat{s}_r(t)$. Squared Pearson's correlation coefficients, ρ_{rs}^2 and ρ_{as}^2 , between the estimates and the true signal in each bottom panel quantify their accuracy. This figure shows the best-case scenario among those in Fig. 3a,b. In shallower gradients or other background concentrations, the discrepancy between ρ_{rs}^2 and ρ_{as}^2 increases to 100-fold or more. **b**, Chemotactic drift speed normalized by swimming speed v_d/v_r as a function of gradient steepness g for ideal cells (blue) and *E. coli* (green) in simulations ($c_0 = 1 \mu\text{M}$; Supplementary Section 14). Error bars in **b** and **c** are s.e.m. about the average of $N \geq 10,000$ simulations, each of duration $T = 100\tau_v$. Lines in **b** and **c** connect simulation points to aid the eye. **c**, Information lost between particle arrivals and kinase activity cause *E. coli* to climb gradients at speeds v_a that are smaller than those of ideal cells v_r by a factor of $(I_{s \rightarrow a}^*/I_{s \rightarrow r}^*)^{1/2}$, where $I_{s \rightarrow a}^*$ and $I_{s \rightarrow r}^*$ are the information rates of *E. coli* and ideal cells, respectively. Blue line: v_a/v_r plotted against $(I_{s \rightarrow a}^*/I_{s \rightarrow r}^*)^{1/2}$ in a parametric plot with varying g . Black dashed line: $y = x$ line for comparison. Dots are $g = \{0.05, 0.1, 0.2, 0.3, 0.4\} \text{ mm}^{-1}$, from top right to bottom left.

background concentrations^{63,64} suppresses response gain in high backgrounds, but the internal noise stays constant, reducing information. Cells may need to amplify signals above downstream noise sources, such as stochastic motor switching, requiring the densely packed arrays seen universally across bacterial species⁶⁶, but strongly coupled CheA kinases probably also introduce noise. Indeed, the dense localization of receptors indicates that molecule counting is not limiting, as if it were, the optimal strategy would be to uniformly distribute the receptors². *E. coli* also need to sense many chemicals⁴⁸ with different receptors, but their presence in the array reduces the response to any one ligand⁶¹. *E. coli* are also probably under selection

pressures to perform other tasks, such as localizing at concentration peaks^{43,67}. The laboratory strain we used, RP437, was originally selected for chemotaxis through collective migration assays^{68–70}, and the steep gradients generated during migration, $g \approx 1 \text{ mm}^{-1}$ or steeper^{71–73}, might obviate the need for a high-fidelity sensor. Last, increasing information about signals may be too costly in resources or energy to be worth the gain in fitness^{11–13,18,22,74}. The mechanism of amplification is not well understood, but recent work has argued that it consumes energy^{75–77}. Further work is needed to distinguish these possibilities.

Although physical limits and normative theories provide useful points of comparison, our results motivate investigations of the system-specific, physical and biological constraints on biological information processing.

Online content

Any methods, additional references, Nature Portfolio reporting summaries, source data, extended data, supplementary information, acknowledgements, peer review information; details of author contributions and competing interests; and statements of data and code availability are available at <https://doi.org/10.1038/s41567-025-03111-4>.

References

- Barlow, H. B. in *Sensory Communication* (ed. Rosenblith, W. A.) 216–234 (MIT Press, 1961).
- Berg, H. C. & Purcell, E. M. Physics of chemoreception. *Biophys. J.* **20**, 193–219 (1977).
- Laughlin, S. A simple coding procedure enhances a neuron's information capacity. *Z. Naturforsch. C* **36**, 910–912 (1981).
- Osborne, L. C., Lisberger, S. G. & Bialek, W. A sensory source for motor variation. *Nature* **437**, 412–416 (2005).
- Chklovskii, D. B., Schikorski, T. & Stevens, C. F. Wiring optimization in cortical circuits. *Neuron* **34**, 341–347 (2002).
- Bialek, W. *Biophysics: Searching for Principles* (Princeton Univ. Press, 2012).
- Petkova, M. D., Tkačík, G., Bialek, W., Wieschaus, E. F. & Gregor, T. Optimal decoding of cellular identities in a genetic network. *Cell* **176**, 844–855 (2019).
- Mattingly, H. H., Kamino, K., Machta, B. B. & Emonet, T. *Escherichia coli* chemotaxis is information limited. *Nat. Phys.* **17**, 1426–1431 (2021).
- Tkačík, G. & Bialek, W. Information processing in living systems. *Annu. Rev. Condens. Matter Phys.* **7**, 89–117 (2016).
- Tkačík, G. & Wolde, P. R. T. Information processing in biochemical networks. *Annu. Rev. Biophys.* **54**, 249–274 (2025).
- Govern, C. C. & Ten Wolde, P. R. Optimal resource allocation in cellular sensing systems. *Proc. Natl Acad. Sci. USA* **111**, 17486–17491 (2014).
- Tjalma, A. J. et al. Trade-offs between cost and information in cellular prediction. *Proc. Natl Acad. Sci. USA* **120**, e2303078120 (2023).
- Lan, G. & Tu, Y. Information processing in bacteria: memory, computation, and statistical physics: a key issues review. *Rep. Prog. Phys.* **79**, 052601 (2016).
- Bryant, S. J. & Machta, B. B. Physical constraints in intracellular signaling: the cost of sending a bit. *Phys. Rev. Lett.* **131**, 068401 (2023).
- Tu, Y. Quantitative modeling of bacterial chemotaxis: signal amplification and accurate adaptation. *Annu. Rev. Biophys.* **42**, 337–359 (2013).
- Parkinson, J. S., Hazelbauer, G. L. & Falke, J. J. Signaling and sensory adaptation in *Escherichia coli* chemoreceptors: 2015 update. *Trends Microbiol.* **23**, 257–266 (2015).
- Berg, H. C. *E. Coli in Motion* (Springer, 2004).

18. Ni, B., Colin, R., Link, H., Endres, R. G. & Sourjik, V. Growth-rate dependent resource investment in bacterial motile behavior quantitatively follows potential benefit of chemotaxis. *Proc. Natl Acad. Sci. USA* **117**, 595–601 (2020).
19. Bialek, W. & Setayeshgar, S. Physical limits to biochemical signaling. *Proc. Natl Acad. Sci. USA* **102**, 10040–10045 (2005).
20. Endres, R. G. & Wingreen, N. S. Maximum likelihood and the single receptor. *Phys. Rev. Lett.* **103**, 158101 (2009).
21. Mora, T. & Wingreen, N. S. Limits of sensing temporal concentration changes by single cells. *Phys. Rev. Lett.* **104**, 248101 (2010).
22. Mehta, P., Lang, A. H. & Schwab, D. J. Landauer in the age of synthetic biology: energy consumption and information processing in biochemical networks. *J. Stat. Phys.* **162**, 1153–1166 (2016).
23. Hein, A. M., Brumley, D. R., Carrara, F., Stocker, R. & Levin, S. A. Physical limits on bacterial navigation in dynamic environments. *J. R. Soc. Interface* **13**, 20150844 (2016).
24. ten Wolde, P. R., Becker, N. B., Ouldridge, T. E. & Mugler, A. Fundamental limits to cellular sensing. *J. Stat. Phys.* **162**, 1395–1424 (2016).
25. Aquino, G., Wingreen, N. S. & Endres, R. G. Know the single-receptor sensing limit? Think again. *J. Stat. Phys.* **162**, 1353–1364 (2016).
26. Mora, T. & Nemenman, I. Physical limit to concentration sensing in a changing environment. *Phys. Rev. Lett.* **123**, 198101 (2019).
27. Colin, R., Rosazza, C., Vaknin, A. & Sourjik, V. Multiple sources of slow activity fluctuations in a bacterial chemosensory network. *eLife* **6**, e26796 (2017).
28. Keegstra, J. M. et al. Phenotypic diversity and temporal variability in a bacterial signaling network revealed by single-cell FRET. *eLife* **6**, e27455 (2017).
29. Kamino, K., Keegstra, J. M., Long, J., Emonet, T. & Shimizu, T. S. Adaptive tuning of cell sensory diversity without changes in gene expression. *Sci. Adv.* **6**, eabc1087 (2020).
30. Kamino, K. et al. Optimal inference of molecular interaction dynamics in FRET microscopy. *Proc. Natl Acad. Sci. USA* **120**, e2211807120 (2023).
31. Moore, J. P., Kamino, K., Kottou, R., Shimizu, T. S. & Emonet, T. Signal integration and adaptive sensory diversity tuning in *Escherichia coli* chemotaxis. *Cell Syst.* **15**, 628–638 (2024).
32. Schreiber, T. Measuring information transfer. *Phys. Rev. Lett.* **85**, 461–464 (2000).
33. Cover, T. M. & Thomas, J. A. *Elements of Information Theory* (Wiley-Interscience, 1991).
34. Long, J., Zucker, S. W. & Emonet, T. Feedback between motion and sensation provides nonlinear boost in run-and-tumble navigation. *PLoS Comput. Biol.* **13**, e1005429 (2017).
35. Das, A. Exact computation of transfer entropy with path weight sampling. *Phys. Rev. Lett.* **135**, 107404 (2025).
36. Hazel, J. R. & Sidell, B. D. A method for the determination of diffusion coefficients for small molecules in aqueous solution. *Anal. Biochem.* **166**, 335–341 (1987).
37. Khursigara, C. M. et al. Lateral density of receptor arrays in the membrane plane influences sensitivity of the *E. coli* chemotaxis response. *EMBO J.* **30**, 1719–1729 (2011).
38. Brumley, D. R. et al. Bacteria push the limits of chemotactic precision to navigate dynamic chemical gradients. *Proc. Natl Acad. Sci. USA* **116**, 10792–10797 (2019).
39. Kolmogorov, A. N. Interpolation and extrapolation of stationary sequences. *Izv. Acad. Sci. USSR* **5**, 3–14 (1941).
40. Wiener, N. *Extrapolation, Interpolation, and Smoothing of Stationary Time Series: With Engineering Applications* (MIT Press, 1949).
41. Hinczewski, M. & Thirumalai, D. Cellular signaling networks function as generalized Wiener-Kolmogorov filters to suppress noise. *Phys. Rev. X* **4**, 041017 (2014).
42. Becker, N. B., Mugler, A. & ten Wolde, P. R. Optimal prediction by cellular signaling networks. *Phys. Rev. Lett.* **115**, 258103 (2015).
43. Celani, A. & Vergassola, M. Bacterial strategies for chemotaxis response. *Proc. Natl Acad. Sci. USA* **107**, 1391–1396 (2010).
44. Reinhardt, M., Tkačík, G. & Ten Wolde, P. R. Path weight sampling: exact Monte Carlo computation of the mutual information between stochastic trajectories. *Phys. Rev. X* **13**, 041017 (2023).
45. Korobkova, E., Emonet, T., Vilar, J. M. G., Shimizu, T. S. & Cluzel, P. From molecular noise to behavioural variability in a single bacterium. *Nature* **428**, 574–578 (2004).
46. Francis, N. R. et al. Subunit organization in a soluble complex of Tar, CheW, and CheA by electron microscopy. *J. Biol. Chem.* **277**, 36755–36759 (2002).
47. Levit, M. N., Grebe, T. W. & Stock, J. B. Organization of the receptor-kinase signaling array that regulates *Escherichia coli* chemotaxis. *J. Biol. Chem.* **277**, 36748–36754 (2002).
48. Yang, Y. et al. Relation between chemotaxis and consumption of amino acids in bacteria. *Mol. Microbiol.* **96**, 1272–1282 (2015).
49. Spudich, J. L. & Koshland, D. E. Non-genetic individuality: chance in the single cell. *Nature* **262**, 467–471 (1976).
50. Park, H. et al. Interdependence of behavioural variability and response to small stimuli in bacteria. *Nature* **468**, 819–823 (2010).
51. Masson, J.-B., Voisinne, G., Wong-Ng, J., Celani, A. & Vergassola, M. Noninvasive inference of the molecular chemotactic response using bacterial trajectories. *Proc. Natl Acad. Sci. USA* **109**, 1802–1807 (2012).
52. Dufour, Y. S., Gillet, S., Frankel, N. W., Weibel, D. B. & Emonet, T. Direct correlation between motile behavior and protein abundance in single cells. *PLoS Comput. Biol.* **12**, e1005041 (2016).
53. Waite, A. J. et al. Non-genetic diversity modulates population performance. *Mol. Syst. Biol.* **12**, 895 (2016).
54. Fu, X. et al. Spatial self-organization resolves conflicts between individuality and collective migration. *Nat. Commun.* **9**, 2177 (2018).
55. Waite, A. J., Frankel, N. W. & Emonet, T. Behavioral variability and phenotypic diversity in bacterial chemotaxis. *Annu. Rev. Biophys.* **47**, 595–616 (2018).
56. Li, L. et al. Phenotypic variability shapes bacterial responses to opposing gradients. *PRX Life* **2**, 013001 (2024).
57. Sourjik, V. & Berg, H. C. Receptor sensitivity in bacterial chemotaxis. *Proc. Natl Acad. Sci. USA* **99**, 123–127 (2002).
58. Monod, J., Wyman, J. & Changeux, J.-P. On the nature of allosteric transitions: a plausible model. *J. Mol. Biol.* **12**, 88–118 (1965).
59. Mello, B. A. & Tu, Y. An allosteric model for heterogeneous receptor complexes: understanding bacterial chemotaxis responses to multiple stimuli. *Proc. Natl Acad. Sci. USA* **102**, 17354–17359 (2005).
60. Keymer, J. E., Endres, R. G., Skoge, M., Meir, Y. & Wingreen, N. S. Chemosensing in *Escherichia coli*: two regimes of two-state receptors. *Proc. Natl Acad. Sci. USA* **103**, 1786–1791 (2006).
61. Sourjik, V. & Berg, H. C. Functional interactions between receptors in bacterial chemotaxis. *Nature* **428**, 437–441 (2004).
62. Moore, J. P., Kamino, K. & Emonet, T. Non-genetic diversity in chemosensing and chemotactic behavior. *Int. J. Mol. Sci.* **22**, 6960 (2021).
63. Kalinin, Y. V., Jiang, L., Tu, Y. & Wu, M. Logarithmic sensing in *Escherichia coli* bacterial chemotaxis. *Biophys. J.* **96**, 2439–2448 (2009).
64. Lazova, M. D., Ahmed, T., Bellomo, D., Stocker, R. & Shimizu, T. S. Response rescaling in bacterial chemotaxis. *Proc. Natl Acad. Sci. USA* **108**, 13870–13875 (2011).
65. Sarkka, S. *Bayesian Filtering and Smoothing* (Cambridge Univ. Press, 2013).

66. Briegel, A. et al. Universal architecture of bacterial chemoreceptor arrays. *Proc. Natl Acad. Sci. USA* **106**, 17181–17186 (2009).
67. Clark, D. A. & Grant, L. C. The bacterial chemotactic response reflects a compromise between transient and steady-state behavior. *Proc. Natl Acad. Sci. USA* **102**, 9150–9155 (2005).
68. Armstrong, J. B., Adler, J. & Dahl, M. M. Nonchemotactic mutants of *Escherichia coli*. *J. Bacteriol.* **93**, 390–398 (1967).
69. Bachmann, B. J. Pedigrees of some mutant strains of *Escherichia coli* K-12. *Bacteriol. Rev.* **36**, 525–557 (1972).
70. Barker, C. S., Prüß, B. M. & Matsumura, P. Increased motility of *Escherichia coli* by insertion sequence element integration into the regulatory region of the *flhD* operon. *J. Bacteriol.* **186**, 7529–7537 (2004).
71. Phan, T. V. et al. Direct measurement of dynamic attractant gradients reveals breakdown of the Patlak-Keller-Segel chemotaxis model. *Proc. Natl Acad. Sci. USA* **121**, e2309251121 (2024).
72. Narla, A. V., Cremer, J. & Hwa, T. A traveling-wave solution for bacterial chemotaxis with growth. *Proc. Natl Acad. Sci. USA* **118**, e2105138118 (2021).
73. Mattingly, H. H. & Emonet, T. Collective behavior and nongenetic inheritance allow bacterial populations to adapt to changing environments. *Proc. Natl Acad. Sci. USA* **119**, e2117377119 (2022).
74. Sartori, P. & Tu, Y. Free energy cost of reducing noise while maintaining a high sensitivity. *Phys. Rev. Lett.* **115**, 118102 (2015).
75. Hathcock, D. et al. A nonequilibrium allosteric model for receptor-kinase complexes: the role of energy dissipation in chemotaxis signaling. *Proc. Natl Acad. Sci. USA* **120**, e2303115120 (2023).
76. Hathcock, D., Yu, Q. & Tu, Y. Time-reversal symmetry breaking in the chemosensory array reveals a general mechanism for dissipation-enhanced cooperative sensing. *Nat. Commun.* **15**, 8892 (2024).
77. Sherry, D. M., Graf, I. R., Bryant, S. J., Emonet, T. & Machta, B. B. Lattice ultrasensitivity produces large gain in *E. coli* chemosensing. Preprint at bioRxiv <https://doi.org/10.1101/2024.05.28.596300> (2024).

Publisher's note Springer Nature remains neutral with regard to jurisdictional claims in published maps and institutional affiliations.

Open Access This article is licensed under a Creative Commons Attribution-NonCommercial-NoDerivatives 4.0 International License, which permits any non-commercial use, sharing, distribution and reproduction in any medium or format, as long as you give appropriate credit to the original author(s) and the source, provide a link to the Creative Commons licence, and indicate if you modified the licensed material. You do not have permission under this licence to share adapted material derived from this article or parts of it. The images or other third party material in this article are included in the article's Creative Commons licence, unless indicated otherwise in a credit line to the material. If material is not included in the article's Creative Commons licence and your intended use is not permitted by statutory regulation or exceeds the permitted use, you will need to obtain permission directly from the copyright holder. To view a copy of this licence, visit <http://creativecommons.org/licenses/by-nc-nd/4.0/>.

© The Author(s) 2026

Methods

Strains and plasmids

All strains and plasmids used are the same as in our previous works^{8,30}. The following quoted text, except citation numbers, is from ref. 8: ‘The strain used for the FRET experiments is a derivative of *E. coli* K-12 strain RP437 (HCB33), a gift of T. Shimizu, and described in detail elsewhere^{28,29}. In brief, the FRET acceptor–donor pair (CheY-mRFP and CheZ-mYFP) is expressed in tandem from plasmid pSJAB106²⁸ under an isopropyl β-D-thiogalactopyranoside (IPTG)-inducible promoter. The glass-adhesive mutant of FliC (FliC*) was expressed from a sodium salicylate (NaSal)-inducible pZR1 plasmid²⁸. The plasmids are transformed in VS115, a *cheY cheZ fliC* mutant of RP437²⁸ (gift of V. Sourjik). ... RP437, the direct parent of the FRET strain and also a gift from T. Shimizu, was used to measure behavioral parameters.’

Cell preparation

Single-cell FRET microscopy and cell culturing were carried out as described previously^{8,28–31}. The following quoted text, except citation numbers, is from ref. 8, with brackets to indicate modified text: ‘Cells were picked from a frozen stock at –80 °C and inoculated in 2 ml of tryptone broth (TB; 1% bacto tryptone, 0.5% NaCl) and grown overnight to saturation at 30 °C and shaken at 250 rpm. Cells from a saturated overnight culture were diluted ×100 in 10 ml TB and grown to OD600 0.45–0.47 in the presence of 100 µg ml^{−1} ampicillin, 34 µg ml^{−1} chloramphenicol, 50 µM IPTG and 3 µM NaSal, at 33.5 °C and 250 rpm shaking. Cells were collected by centrifugation (5 min at 5,000 rpm, or [\times 4,080g]) and washed [once] with motility buffer (10 mM KPO₄, 0.1 mM EDTA, 1 µM methionine, 10 mM lactic acid, pH 7), and then were resuspended in 2 ml motility buffer’ plus the final concentration of Asp. ‘Cells were left at 22 °C for 90 min before loading into the microfluidic device. All experiments, FRET and swimming, were performed at 22–23 °C.

‘For swimming ... experiments, cells were prepared identically. Saturated overnight cultures were diluted ×100 in 5 ml of TB. After growing to OD600 0.45–0.47, 1 ml of cell suspension was washed twice in motility buffer with 0.05% w/v of polyvinylpyrrolidone (MW 40 kDa) (PVP-40) added. Washes were done by centrifuging the suspension in an Eppendorf tube at [\times 1,700g] (4,000 rpm in this centrifuge) for 3 min. After the last wash, cells were resuspended with varying [background] concentrations of [Asp].’

Microfluidic device fabrication and loading for FRET measurements

Microfluidic devices for the FRET experiments^{29–31} were made from polydimethylsiloxane on 24 60-mm cover glasses (No. 1.5) following standard soft lithography protocols⁷⁸, as done before⁸.

Sample preparation in the microfluidic device was conducted as before⁸. The following quoted text is from ref. 8, with brackets to indicate modified text: ‘Five inlets of the device ... were connected to reservoirs (Liquid chromatography columns, C3669; Sigma Aldrich) filled with motility buffer containing various concentrations of [Asp] through polyethylene tubing (Polythene Tubing, 0.58 mm id, 0.96 mm od; BD Intermedic) [see the Supplementary Information in ref. 8]. The tubing was connected to the PMDS device through stainless steel pins that were directly plugged into the inlets or outlet of the device (New England Tubing). Cells washed and suspended in motility buffer were loaded into the device from the outlet and allowed to [attach] to the cover glass surface via their sticky flagella by reducing the flow speed inside the chamber. The pressure applied to the inlet solution reservoirs was controlled by computer-controlled solenoid valves (MH1; Festo), which rapidly switched between atmospheric pressure and higher pressure (1.0 kPa) using a source of pressurized air. Only one experiment was conducted per device.’ *E. coli* consume Asp, so all experiments below were performed with a low dilution of cells to minimize this effect. The continuous flow of fresh media also helped

ensure that consumption of Asp minimally affected the signal that cells experienced.

Single-cell FRET imaging system

FRET imaging in the microfluidic device was performed using the same set-up as before^{8,30}. The following quoted text, except citation numbers, is from ref. 8: ‘FRET imaging in the microfluidic device was performed using an inverted microscope (Eclipse Ti-E; Nikon) equipped with an oil-immersion objective lens (CFI Apo TIRF 60X Oil; Nikon). YFP was illuminated by an LED illumination system (SOLA SE, Lumencor) through an excitation bandpass filter (FF01-500/24-25; Semrock) and a dichroic mirror ([FF520-Di02-25x36]; Semrock). The fluorescence emission was led into an emission image splitter (OptoSplit II; Cairn) and further split into donor and acceptor channels by a second dichroic mirror (FF580-FDi01-25x36; Semrock). The emission was then collected through emission bandpass filters ([FF01-542/27-25] and [FF02-641/75-25]; Semrock) by a sCMOS camera (ORCA-Flash4.0 V2; Hamamatsu). RFP was illuminated in the same way as YFP except that an excitation bandpass filter (FF01-575/05-25; Semrock) and a dichroic mirror (FF593-Di03-25x36; Semrock) were used. An additional excitation filter (59026X; Chroma) was used in front of the excitation filters. To synchronize image acquisition and the delivery of stimulus solutions, a custom-made MATLAB program controlled both the imaging system (through the API provided by Micro-Manager⁷⁹) and the states of the solenoid valves.’

Computing FRET signal and kinase activity

FRET signals were extracted from raw images using the E-FRET method⁸⁰, an analysis method for FRET data that corrects for different rates of photobleaching between donor and acceptor molecules. In this method, YFP (the donor) is illuminated and YFP emission images (I_{DD}) and RFP (the acceptor) emission images (I_{DA}) are captured. Periodically, RFP was illuminated and RFP emission images were captured (I_{AA}). From these, the photobleach-corrected FRET signal was computed as before⁸. This is related to the kinase activity $a(t)$ by an affine transform when CheY and CheZ are overexpressed^{8,57}. All parameters associated with the imaging system were measured previously⁸.

In each experiment, we first delivered a short saturating stimulus (1 mM MeAsp plus 100 µM serine⁶¹) to determine the FRET signal at minimum kinase activity, which was followed by a motility buffer with Asp at background concentration c_0 . Before the saturating stimulus was delivered, the donor was excited every 0.5 s to measure I_{DD} and I_{DA} for 5 s (see the Supplementary Information in ref. 8). Then the stimulus was delivered for 10 s, and the donor was excited every 0.5 s during this time. Before and after the donor excitations, the acceptor was excited three times in 0.5-s intervals to measure I_{AA} (see the Supplementary Information in ref. 8). After the stimulus was removed, the acceptor was excited three more times at 0.5-s intervals. Imaging was then stopped and cells were allowed to adapt to the background for 120 s.

Stimulus protocols for measuring kinase linear response functions and fluctuations are described below.

At the end of each experiment, we delivered a long saturating stimulus (1 mM MeAsp plus 100 µM serine) for 180 s to allow the cells to adapt. Then we removed the stimulus back to the background concentration, eliciting a strong response from the cells, from which we determined the FRET signal at maximum kinase activity. The donor was excited for 5 s before the saturating stimulus and 10 s after it, every 0.5 s. Before and after these donor excitations, the acceptor was excited three times in 0.5-s intervals. The cells were exposed to the saturating stimulus for 180 s. The donor was excited every 0.5 s for 5 s before cells were exposed to the motility buffer with Asp at background concentration c_0 , followed by 10 s of further donor excitations. Before and after the donor excitations, the acceptor was again excited three times in 0.5-s intervals.

FRET signals were extracted as before⁸. The FRET signal at minimum kinase activity FRET_{min} was computed from the average FRET

signal during the first saturating stimulus. The FRET signal at maximum kinase activity $FRET_{max}$ was computed from the average FRET signal during the first quarter (2.5 s) of the removal stimulus at the end of the experiment. Kinase activity was then computed from corrected FRET signal: $a(t) = \frac{FRET(t) - FRET_{min}}{FRET_{max} - FRET_{min}}$.

Kinase linear response functions

Experiments were performed in Asp background concentrations c_0 of 0.1 μM , 1 μM and 10 μM . Measurements were made in single cells, and at least three biological replicates were performed per background. The FRET level at the minimum kinase activity was measured at the beginning of each experiment, as described above. After this, a series of stimuli were delivered to the cells in the microfluidic device. Cells were illuminated and imaged only when stimulated to limit photobleaching. Before each stimulus, cells were imaged for 7.5 s in the background concentration c_0 . Then, the concentration of Asp was shifted up to $c_+ > c_0$ for 30 s and imaging continued. The donor excitation interval was 0.75 s, and acceptor excitations were done before and after the set of donor excitations. After this, imaging was stopped and the Asp concentration returned to c_0 for 65 s to allow cells to adapt. Then, the same process was repeated, but this time with the Asp concentration shifted down to $c_- < c_0$. Alternating up and down stimuli were repeated 10 times each. c_+ and c_- varied with each experiment and each background c_0 . Finally, the FRET level at maximum kinase activity was measured at the end of each experiment, as described above. The whole imaging protocol lasted <2,200 s. In total, cells spent <60 min in the device, from loading to the end of imaging.

These data were analysed as before⁸ to extract linear response parameters for each cell. In brief, the responses of a cell to all steps up or steps down in concentration were averaged and the standard error of the response at each time point computed. Model parameters were extracted by maximizing the posterior probability of parameters given data, assuming a Gaussian likelihood function and log-uniform priors for the parameters. The uncertainties of single-cell parameter estimates were generated by Markov chain Monte Carlo sampling the posterior distribution. Finally, the population-median parameters were computed from all cells in experiments in a given background c_0 . The uncertainty $\sigma_{\theta_i}^2$ of the population-median value of parameter θ_i , with $\theta = (G, \tau_1, \tau_2)$, was computed using:

$$\sigma_{\theta_i}^2 = \frac{1}{N} (1.4826 \text{ mad}(\{\theta_i^{\text{MAP}}\}))^2 + \frac{1}{N^2} \sum_k (\sigma_{\theta_i|k}^2). \quad (5)$$

This expression accounts both for cell-to-cell variations (first term) and uncertainties in the single-cell estimates (second term). N is the number of cells, and 1.4826 $\text{mad}(\cdot)$ is an outlier-robust uncertainty estimate that coincides with the standard deviation when the samples are Gaussian distributed, where $\text{mad}(\cdot)$ is the median absolute deviation, as used previously⁸. $\{\theta_i^{\text{MAP}}\}$ are the single-cell maximum a posteriori estimates of parameter θ_i . $(\sigma_{\theta_i|k}^2)$ is the uncertainty of θ_i^{MAP} in cell k , which was computed using

$$(\sigma_{\theta_i|k}) = 1.4826 \text{ mad}(\{\hat{\theta}_i|k\}), \quad (6)$$

where $\{\hat{\theta}_i|k\}$ are the samples from the posterior of the k th cell using a Markov chain Monte Carlo approach.

Fitting the MWC kinase gain

Parameters G_∞ and K_1 in the MWC model gain were estimated by fitting the model to estimated values of G in each background c_0 . The fit was done by minimizing the sum of squared errors between the logarithms of the measured G and the predicted values of G . As the estimated values of G varied by about an order of magnitude, taking the logarithms ensured that the smallest value of G had a similar weight as the largest value in the objective function.

Statistics of noise in kinase activity

Fluctuations in kinase activity were measured in the same Asp background concentrations c_0 as above, as well as $c_0 = 0 \mu\text{M}$. At least three replicate experiments were performed per background. The FRET level at minimum kinase activity was measured at the beginning of each experiment, as described above. After these measurements, imaging was then stopped and cells were allowed to adapt to the background for 120 s. After this, cells were imaged for about 1,200 s. Throughout, donor excitations were done every 1.0 s, except when it was interrupted by acceptor excitations, which were conducted every 100 donor excitations (see the Supplementary Information in ref. 8). Finally the FRET level at maximum kinase activity was measured at the end of each experiment, as described above. The whole imaging protocol lasted <1,400 s. In total, cells spent about <60 min in the device, from loading to the end of imaging.

These data were analysed as before⁸. Bayesian filtering methods⁶⁵ were used to compute the likelihood of the parameters given the data, and the prior distribution was taken to be uniform in log. Single-cell estimates and uncertainties of the noise parameters were extracted from the posterior distribution as described above. The population-median parameter values were computed in each background c_0 , and their uncertainties were computed as described above, with $\theta = (D_n, \tau_n)$.

Swimming velocity statistics

Cells were prepared and imaged as before⁸. After the second wash step described in ‘Cell preparation’, the cells were centrifuged again and resuspended in the motility buffer containing a background concentration of Asp c_0 . The values of c_0 used here were the same as in the FRET experiments, including $c_0 = 0 \mu\text{M}$. Then, the cell suspension was diluted to an OD600 of 0.00025. This low dilution of cells both enabled tracking and minimized the effect of cells consuming Asp. The cell suspension was then loaded into μ -slide chemotaxis devices (Ibidi). Swimming cells were tracked in one of the large reservoirs. Moreover, 1,000-s videos of swimming cells were recorded on a Nikon Ti-E Inverted Microscope using a CFI Plan Fluor $\times 4$ objective (numerical aperture 0.13). Images were captured using a sCMOS camera (ORCA-Flash4.0 V2; Hamamatsu). Four biological replicates were performed for each background c_0 .

Cell detection and tracking were carried out using the same custom MATLAB script as we used previously⁸, with the same analysis parameters (see the Supplementary Information of that paper for details). Tumble detection was also carried out identically as before⁸. There was no minimum trajectory duration, but cells were kept only if at least two tumbles were detected in their trajectory. For each cell, we computed the fraction of time spent in the ‘run’ state P_{run} . Then we constructed the distribution of P_{run} , correcting for biases caused by the different diffusivities of cells with different P_{run} . We then computed the correlation function of velocity along one spatial dimension for each cell, $V_i(t) = \langle v_x(t') v_x(t' + t) \rangle_t$, among cells with P_{run} within ± 0.01 of the population-median value. Finally, we computed a weighted average of the correlation functions over all cells in the population-median bin of P_{run} , where trajectories were weighted by their duration, giving $V(t)$. In each background c_0 , for the median bin of P_{run} , the average trajectory duration was ~ 7.6 s, and the total trajectory time was $\geq 2.7 \times 10^4$ s.

These correlation functions $V(t)$ in each background c_0 and each experiment were fitted to decaying exponentials $\sigma_v^2 \exp(-|t|/\tau_v)$, and the parameters and their uncertainties were extracted in two steps. First, we determined the maximum a posteriori estimates of the parameters. The parameters were initially estimated using the MATLAB fit function to fit exponentials to $V(t)$ in the time range $t \in [2\Delta t, 10 \text{ s}]$, with $\Delta t = 50 \text{ ms}$. The estimated τ_v was used to get the uncertainty of $V(t)$ in each experiment. Assuming a Gaussian likelihood function and parameters distributed uniformly in logarithm, the posterior distributions of the parameters were constructed. In each experiment, maximum a posteriori estimates of the parameters were extracted as done for the

kinase parameters, and parameter uncertainties were computed from Markov chain Monte Carlo samples of the posterior distribution as above. Finally, we computed the average parameters σ_v^2 and τ_v over experimental replicates, as well as their standard errors over replicates.

Further error analysis

Once the variance of the population-median value of parameter i was computed, $\sigma_{\theta_i}^2$, we propagated the uncertainty to functions of those parameters. For some function of the parameters $f(\theta)$, we computed its variance, σ_f^2 , as:

$$\begin{aligned}\sigma_f^2 &= \sum_i \left(\frac{\partial f}{\partial \theta_i} \right)^2 \sigma_{\theta_i}^2 \\ &= f^2 \sum_i \left(\frac{\partial \log f}{\partial \theta_i} \right)^2 \sigma_{\theta_i}^2.\end{aligned}\quad (7)$$

The equations above neglect correlations in the uncertainties between pairs of parameters. This formula was used to compute the uncertainties of $I_{s \rightarrow r}^*$, $I_{s \rightarrow a}^*$ and η . The same formula was used to compute uncertainties in functions of time by applying it pointwise at each time delay t and neglecting correlations in uncertainties between time points.

Data were collected using MATLAB 2021 and Micro-Manager 2.0.0. Data were analysed and simulations were performed using MATLAB 2022b. At least three biological replicates were performed per condition, corresponding to about 100 cells per condition, to estimate parameter uncertainties. No method was used to predetermine the sample size. No statistical tests were performed. In the FRET experiments, cells whose kinase activity left the range 0 to 1 by more than 0.2 were excluded from the analysis.

Reporting summary

Further information on research design is available in the Nature Portfolio Reporting Summary linked to this article.

Data availability

Data shown in the main text figures are included as Supplementary Data.

Code availability

Code that can be used to reproduce the main text figures, including the simulation code, are included as Supplementary Code. All algorithms are described in detail in Supplementary Information.

References

- 78. Qin, D., Xia, Y. & Whitesides, G. M. Soft lithography for micro- and nanoscale patterning. *Nat. Protoc.* **5**, 491–502 (2010).
- 79. Edelstein, A., Amodaj, N., Hoover, K., Vale, R. & Stuurman, N. Computer control of microscopes using μManager. *Curr. Protoc. Mol. Biol.* **92**, 14.20.1–14.20.17 (2010).
- 80. Zal, T. & Gascoigne, N. R. J. Photobleaching-corrected FRET efficiency imaging of live cells. *Biophys. J.* **86**, 3923–3939 (2004).

Acknowledgements

We thank T. Shimizu and V. Sourjik for bacteria strains. We also thank J. Moore for help with the experimental assay. This work was supported by the Alfred P. Sloan Foundation (grant no. G-2023-19668 to H.H.M., T.E. and B.B.M.), by the National Institutes of Health (NIH) (awards R01GM138533 and R35GM158058 to T.E. and R35GM138341 to B.B.M.), by a Simons Investigator Award 624156 (B.B.M.), by a Japan Science and Technology Agency Precursory Research for Embryonic Science and Technology (JST PRESTO) grant JPMJPR21E4 (K.K.) and by the Taiwan National Science and Technology Council (NSTC) (grant no. 112-2112-M-001-080-MY3 to K.K.). H.H.M. was supported by the Simons Foundation. K.K. was also supported by the Institute of Molecular Biology, Academia Sinica.

Author contributions

B.B.M. and H.H.M. conceived of the project. K.K., H.H.M., T.E. and B.B.M. designed the experiments. K.K., J.O., R.K. and H.H.M. performed the experiments. H.H.M. and K.K. analysed the data. H.H.M. and B.B.M. derived the theoretical results. H.H.M. wrote the first draft of the paper. H.H.M., B.B.M., K.K. and T.E. edited the paper.

Competing interests

The authors declare no competing interests.

Additional information

Supplementary information The online version contains supplementary material available at <https://doi.org/10.1038/s41567-025-03111-4>.

Correspondence and requests for materials should be addressed to Henry H. Mattingly, Thierry Emonet or Benjamin B. Machta.

Peer review information *Nature Physics* thanks the anonymous reviewers for their contribution to the peer review of this work.

Reprints and permissions information is available at www.nature.com/reprints.

Reporting Summary

Nature Portfolio wishes to improve the reproducibility of the work that we publish. This form provides structure for consistency and transparency in reporting. For further information on Nature Portfolio policies, see our [Editorial Policies](#) and the [Editorial Policy Checklist](#).

Statistics

For all statistical analyses, confirm that the following items are present in the figure legend, table legend, main text, or Methods section.

n/a Confirmed

- The exact sample size (n) for each experimental group/condition, given as a discrete number and unit of measurement
- A statement on whether measurements were taken from distinct samples or whether the same sample was measured repeatedly
- The statistical test(s) used AND whether they are one- or two-sided
Only common tests should be described solely by name; describe more complex techniques in the Methods section.
- A description of all covariates tested
- A description of any assumptions or corrections, such as tests of normality and adjustment for multiple comparisons
- A full description of the statistical parameters including central tendency (e.g. means) or other basic estimates (e.g. regression coefficient) AND variation (e.g. standard deviation) or associated estimates of uncertainty (e.g. confidence intervals)
- For null hypothesis testing, the test statistic (e.g. F , t , r) with confidence intervals, effect sizes, degrees of freedom and P value noted
Give P values as exact values whenever suitable.
- For Bayesian analysis, information on the choice of priors and Markov chain Monte Carlo settings
- For hierarchical and complex designs, identification of the appropriate level for tests and full reporting of outcomes
- Estimates of effect sizes (e.g. Cohen's d , Pearson's r), indicating how they were calculated

Our web collection on [statistics for biologists](#) contains articles on many of the points above.

Software and code

Policy information about [availability of computer code](#)

Data collection Data was collected using MATLAB 2021 and Micro-Manager 2.0.0.

Data analysis Data was analyzed and simulations were performed using MATLAB 2022b.

For manuscripts utilizing custom algorithms or software that are central to the research but not yet described in published literature, software must be made available to editors and reviewers. We strongly encourage code deposition in a community repository (e.g. GitHub). See the Nature Portfolio [guidelines for submitting code & software](#) for further information.

Data

Policy information about [availability of data](#)

All manuscripts must include a [data availability statement](#). This statement should provide the following information, where applicable:

- Accession codes, unique identifiers, or web links for publicly available datasets
- A description of any restrictions on data availability
- For clinical datasets or third party data, please ensure that the statement adheres to our [policy](#)

Data shown in the main text figures are included as Supplementary Data.

Research involving human participants, their data, or biological material

Policy information about studies with [human participants or human data](#). See also policy information about [sex, gender \(identity/presentation\), and sexual orientation](#) and [race, ethnicity and racism](#).

| | |
|--|---|
| Reporting on sex and gender | <input type="checkbox"/> Not applicable |
| Reporting on race, ethnicity, or other socially relevant groupings | <input type="checkbox"/> Not applicable |
| Population characteristics | <input type="checkbox"/> Not applicable |
| Recruitment | <input type="checkbox"/> Not applicable |
| Ethics oversight | <input type="checkbox"/> Not applicable |

Note that full information on the approval of the study protocol must also be provided in the manuscript.

Field-specific reporting

Please select the one below that is the best fit for your research. If you are not sure, read the appropriate sections before making your selection.

Life sciences Behavioural & social sciences Ecological, evolutionary & environmental sciences

For a reference copy of the document with all sections, see nature.com/documents/nr-reporting-summary-flat.pdf

Life sciences study design

All studies must disclose on these points even when the disclosure is negative.

| | |
|-----------------|--|
| Sample size | At least three biological replicates were performed per condition, corresponding to >80 cells per condition, to estimate parameter uncertainties. No method was used to predetermine sample size. No statistical tests were performed. |
| Data exclusions | In the FRET experiments, cells whose kinase activity left the range 0 to 1 by more than 0.2 were excluded from the analysis. |
| Replication | Replicate experiments gave similar results. |
| Randomization | Not applicable. |
| Blinding | Not applicable. |

Reporting for specific materials, systems and methods

We require information from authors about some types of materials, experimental systems and methods used in many studies. Here, indicate whether each material, system or method listed is relevant to your study. If you are not sure if a list item applies to your research, read the appropriate section before selecting a response.

Materials & experimental systems

| | |
|-------------------------------------|--|
| n/a | Involved in the study |
| <input checked="" type="checkbox"/> | <input type="checkbox"/> Antibodies |
| <input checked="" type="checkbox"/> | <input type="checkbox"/> Eukaryotic cell lines |
| <input checked="" type="checkbox"/> | <input type="checkbox"/> Palaeontology and archaeology |
| <input checked="" type="checkbox"/> | <input type="checkbox"/> Animals and other organisms |
| <input checked="" type="checkbox"/> | <input type="checkbox"/> Clinical data |
| <input checked="" type="checkbox"/> | <input type="checkbox"/> Dual use research of concern |
| <input checked="" type="checkbox"/> | <input type="checkbox"/> Plants |

Methods

| | |
|-------------------------------------|---|
| n/a | Involved in the study |
| <input checked="" type="checkbox"/> | <input type="checkbox"/> ChIP-seq |
| <input checked="" type="checkbox"/> | <input type="checkbox"/> Flow cytometry |
| <input checked="" type="checkbox"/> | <input type="checkbox"/> MRI-based neuroimaging |

Plants

Seed stocks

Not applicable.

Novel plant genotypes

Not applicable.

Authentication

Not applicable.